

Magnetically Tunable Optical Metamaterials and Diffractive Robotics

CNF Project Number: 900-00

Principal Investigator(s): Paul L. McEuen^{1,2}

User(s): Conrad L. Smart¹, Tanner G. Pearson³, Zexi Liang^{1,2}, Melody Lim^{1,2}

Affiliation(s): 1. Laboratory of Atomic and Solid-State Physics, 2. Kavli Institute for Nanoscale Science, 3. School of Applied and Engineering Physics; Cornell University

Primary Source(s) of Research Funding: NSF grant DMR-1921567, Air Force Office of Scientific Research (AFSOR) grant FA2386-13-1-4118, CCMR through NSF MRSEC program (DMR-1719875), and the Kavli Institute at Cornell for Nanoscale Science

Contact: plm23@cornell.edu, cs2239@cornell.edu, tgp34@cornell.edu, zl467@cornell.edu, mxl3@cornell.edu

Primary CNF Tools Used: Oxford FlexAL ALD, ASML DUV Stepper, JEOL 6300, CVC E-Beam Evaporators, Oxford 81/82/100 Etchers, PT770/PT740 Etchers, Anatech Asher, Zeiss SEMs, Veeco AFM, Tencor P7 Profilometer, Filmetrics UV, AJA Sputterer

Abstract:

We integrate ultra-flexible, five nanometer thick atomic layer deposition glass hinges with rigid magnetically programmed panels to create untethered, magnetically tunable optical metamaterials and robots at the diffraction limit. We first present a simple walking magnetic microbot consisting of two panels that form a simple mountain-valley fold in an external magnetic field. Next, we fabricate several larger optical metamaterials with magnetically tunable periodicities using this same mountain-valley motif. These structures form the basis for a new class of untethered, microscale optical robots that dynamically interact with the local surroundings (locomotion) and incident light (diffraction).

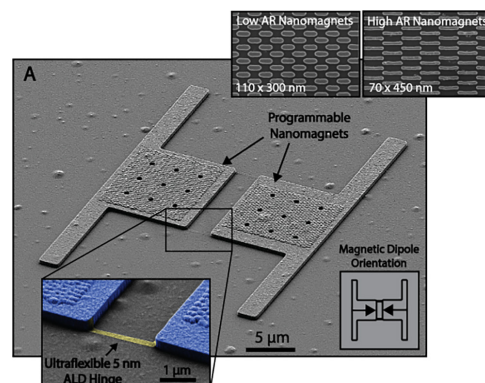


Figure 1: (A) SEM of magnetic microbot. (top-right inset). Arrays of low/high AR nanomagnets used to program the microbot. (bottom-right inset) Final magnetization of the microbot (lower-left zoom). False-color SEM of ALD hinge.

Summary of Research:

Figure 1 shows a microbot at the diffraction limit capable of magnetically controlled locomotion. We first fabricate arrays of single-domain cobalt nanomagnets (top inset) ~ 100 nm on a side with varying aspect ratios (ARs) that form magnetic dipoles along the long axis of the magnets. The coercive fields and magnetic dipole directions of these nanomagnet arrays are tied to the shape anisotropy; since moments prefer to align along the long axis of the magnet, higher shape anisotropy (higher AR) magnets require higher coercive fields. For example, the nanomagnets in Figure 1 (top inset) have coercive fields of 90 mT and 150 mT for the low AR and high AR magnets, respectively. We sequentially magnetize these arrays of nanomagnets with disparate coercive fields to program the magnetic control mechanism of the microbot [1]. The final magnetization directions of the microbot are shown in the bottom-right inset of Fig. 1.

We embed these nanomagnets in rigid glass panels and connect the glass panels together with nanometer thick atomic layer deposition (ALD) glass hinges (lower left, Figure 1) that form a kind of fascia strong enough to hold together the body of the microbot but flexible enough to bend under an external torque [2]. We apply a uniform out-of-plane external field to torque both panels up or down, demonstrating the basic mountain-valley fold essential for origami-inspired metamaterials.

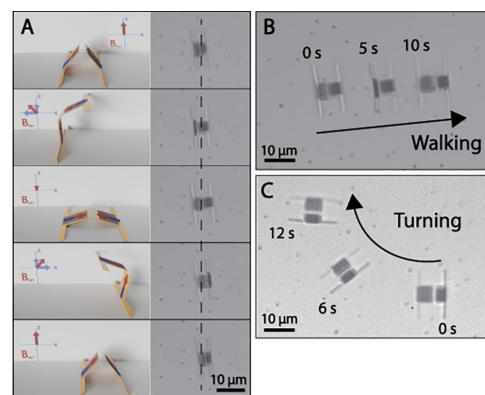


Figure 2: (A) Step motion of the magnetic microbot controlled by sinusoidal external magnetic torque. (B-C) Locomotion of the inchworm with a combination of a 1 Hz sinusoidal z-axis and x-axis magnetic field out-of-phase by 90 degrees. (C) Controlled turning locomotion.

Moreover, we demonstrate a crawling motion that mimics an inchworm by applying a combination of sinusoidal in-plane and out-of-plane magnetic fields out-of-phase by 90 degrees. The stepwise motion of the crawl is depicted in Figure 2A. The main mechanism of walking relies on the extension/contraction of the front/back armature as the microbot pivots out-of-plane. Each step moves the microbot about one-half body length; Figure 2B shows a timelapse of the microbot moving across the substrate with a 1 Hz sinusoidal field over 10 seconds moving at 0.5 body-lengths/second. Faster walking speeds are achieved by increasing the frequency of the control fields. Directional motion and turning (Figure 2C) of the microbot is achieved by adjusting the parity of the in-plane fields.

The simple mountain-valley motif of the microbot is extended to an array of mountain-valley folds to create magnetically tunable optical metamaterials.

For example, Figure 3A shows a linear diffraction grating with a line spacing of 0.5 lines/micron that consists of an array of rigid panels with alternating magnetic dipole orientations (Figure 3A, top-right inset) held together by ALD hinges (Figure 3A, bottom inset). An external out-of-plane field of < 5 mT torques the panels out-of-plane (Figure 3B), and the ALD hinges bend elastically to accommodate this motion contracting and reducing the periodicity of the grating (Figure 3C, left). This contraction can be seen clearly by examining the diffraction peaks in the Fourier plane (Figure 3C, right) when illuminating the gratings with a laser. The first-order diffractive peak ($n=1$) moves away from the central peak as the periodicity of the grating decreases when compressed.

Finally, we apply this same mountain-valley motif to larger, less periodic structures. Figure 4A shows a micrograph of a microbot $50 \mu\text{m}$ on a side consisting of 25 panels, 20 magnetized panels, 4 magnetization directions, all held together by nanometer-thick ALD hinges [3]. The armature structure consists of four arms extending outward from a central panel, with three panels at the end of each arm forming a claw. The dipole orientations are shown in Figure 4B. An external out-of-plane field torques the panels out-of-plane, and the entire structure contracts in two-dimensions (Figure 4C). Finally, we can walk the microbot along the surface using the same crawling motion depicted in Figure 2A. Figure 4D shows a time lapse of the microbot walking along the surface, including a 90-degree turn.

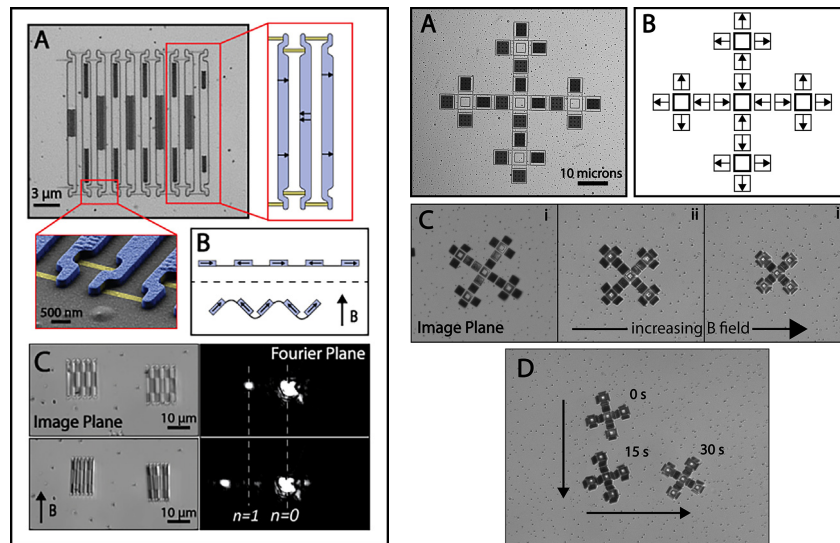


Figure 3, above left: (A) Diffraction grating with magnetically tunable periodicity. (B) Schematic of grating mountain-valley fold. (C) Image (left) and diffraction image (right) of the grating before and after actuation. Figure 4, above right: (A) Micrograph of optical metamaterial with magnetic armature. (B) Programmed magnetic dipole directions. (C) Actuation of the microbot with an increasing out-of-plane external magnetic field from left to right, and (D) locomotion of the microbot, including a 90-degree change of direction.

Conclusions and Future Steps:

The combination of magnetic tunability and ultra-flexible hinges enable a new class of optical metamaterials and microbots at the diffraction limit that provide a new method to actively shape and control incident light using external magnetic fields. Future designs of these optical metamaterials will take the control of light a step further by fabricating optical meta-atoms, subwavelength dielectric optical elements that form the basis of metasurfaces, onto the surface of the microbots. We anticipate incredible potential in numerous fields from local Raman spectroscopy to medical imaging.

Acknowledgements:

This work was performed in part at the Cornell NanoScale Facility (CNF), a member of the NNCI, which is supported by the National Science Foundation (Grant NNCI-2025233).

References:

- [1] J. Cui, et al., Nature 2019, 575, 164.
- [2] K. J. Dorsey, et al., Adv. Mater. 2019, 31, 1901944.
- [3] Kim, Y, et al., Nature 558.7709 (2018): 274-279.

Characterizing Diamond Thin-Film Bulk Acoustic Resonators for Quantum Control

CNF Project Number: 2126-12

Principal Investigator(s): Gregory Fuchs¹

User(s): Johnathan Kuan², Anthony D'Addario²

Affiliation(s): 1. Department of Applied and Engineering Physics, Cornell University;

2. Department of Physics, Cornell University

Primary Source(s) of Research Funding: Defense Advanced Research Projects Agency

- DARPA DRINQS program (Cooperative Agreement #D18AC00024)

Contact: gdf9@cornell.edu, jk2788@cornell.edu, ajd344@cornell.edu

Website: <https://fuchs.research.engineering.cornell.edu/>

Primary CNF Tools Used: OEM Endeavor M1, Westbond 7400A Ultrasonic Wire Bonder

Abstract:

Electro-mechanical resonators have been used to coherently control electron spins in solid-state defect centers such as the nitrogen-vacancy center in diamond. These resonators introduce strain into the diamond lattice, which can be used to drive magnetically-forbidden transitions of the defect center. Strong AC strain driving with these resonators can enhance the spin coherence of the electron spins. To achieve strong AC strain driving, we fabricate a diamond thin-film bulk acoustic resonator and characterize its electromechanical performance. In addition, we use x-ray diffraction to image the ac strain produced by our device, to better understand the device performance.

Summary of Research:

The diamond nitrogen-vacancy (NV) center is a point defect center in the diamond lattice that consists of a substitutional nitrogen atom adjacent to a lattice vacancy. The NV center has been demonstrated to couple to external fields, making it an excellent platform for quantum sensing (e.g., magnetometry, thermometry, strain). In previous experiments, it has been demonstrated that ac lattice strain is an effective mechanism for manipulating the electron spin of the nitrogen-vacancy center. Oscillating lattice strain has been used to coherently drive the electron spin between magnetically forbidden transitions [1,2], which can dynamically decouple the NV center from magnetic noise to enhance its spin coherence [3]. To achieve this dynamical decoupling in a variety of NV center applications, we require strong ac strain driving, which we implement using a diamond thin-film bulk acoustic resonator.

We fabricate a thin-film bulk acoustic resonator (FBAR) on single crystal diamond (Figure 1). The FBAR consists of a transducer stack of AlN (1.5 μm) that is sandwiched between a bottom and top Pt electrode. This transducer sits on a 10 μm optical-grade diamond membrane that is thinned through reactive-ion etching. The AlN film is deposited with the OEM Endeavor M1 tool at CNF.

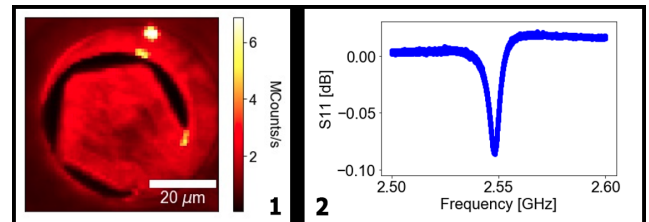


Figure 1, left: Photoluminescence image of the diamond FBAR. The FBAR sits on top of a pentagonal diamond membrane (10 μm) and consists of a Pt bottom electrode, AlN film (1.5 μm), and a top Al electrode. Figure 2, right: S11 measurement of the 2.54 GHz acoustic mode of the AlN FBAR.

In addition, we fabricate an antenna surrounding the FBAR, which allows for magnetic control of the NV center spins in the diamond membrane.

We characterize the electromechanical properties of the FBAR device by measuring the S11 response with a vector network analyzer. We measure a resonance mode at 2.54 GHz, which has a quality factor of 200 (Figure 2). To demonstrate coherent strain driving of a mechanically-forbidden double quantum transition ($m_s = -1$ to $m_s = +1$), we first perform spectroscopy to identify the resonant external magnetic field. We sweep the external field,

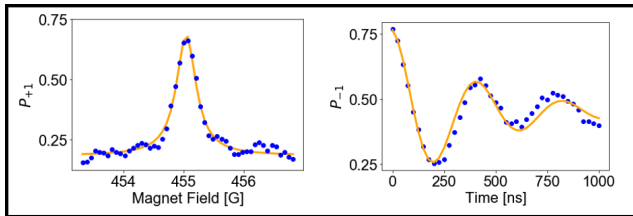


Figure 3: Spectroscopy of the magnetically-forbidden double quantum transition and coherent Rabi driving of the double quantum transition. The spectroscopy sweeps the external magnetic field to tune the Zeeman splitting between $m = -1$ and $m = +1$ to be resonant with the FBAR mode. Rabi oscillations are measured at this field with a Rabi frequency of 2.5 MHz.

which tunes the Zeeman splitting between $m_s = -1$ and $m_s = +1$, while driving the FBAR mode. At this resonant field, we use the FBAR to drive Rabi oscillations between the $m = -1$ and $m = +1$ transition (Figure 3). For this mode, we achieve a Rabi frequency of 2.5 MHz.

We use the Advanced Photon Source at Argonne National Laboratory to measure the strain in the bulk of our FBARs directly with x-rays. We measure the x-ray diffraction of the diamond device using pulsed synchrotron x-rays. We quantify the static strain created during fabrication by comparing the collected diffraction patterns on and off the FBAR region. We can also measure the dynamic ac strain while actively driving the transducer. We collect throughout the entire bulk of the diamond with the X-ray diffraction, which has two full oscillations of the strain wave due to the diamond thickness and mode frequency. As we change the phase of the driving voltage, we observe a peak separate and recombine in the detector images, which quantifies the stroboscopic strain within

the device. Figure 4 shows the mode confinement at the center of the FBAR, which is found by computing the lateral variance subtracted from a reference image for each phase value

Conclusions and Future Steps:

We fabricate and characterize an electro-mechanical mode an AlN diamond thin-film acoustic resonator. We perform spectroscopy to tune double quantum transition of the NV center to be resonant with the FBAR mode and demonstrate coherent strain driving with a Rabi frequency of 1.7 MHz. In addition, to understand the spatial distribution of strain in the FBAR device, we image the FBAR mode with X-ray diffraction and show mode confinement. To improve the performance of our device, we are increasing the size of the device to improve the quality factor and impedance matching.

References:

- [1] E. R. MacQuarrie, T. A. Gosavi, N. R. Jungwirth, S. A. Bhave, and G. D. Fuchs, Mechanical spin control of nitrogen-vacancy centers in diamond, *Phys. Rev. Lett.* 111, 227602 (2013).
- [2] E. R. MacQuarrie, T. A. Gosavi, A. M. Moehle, N. R. Jungwirth, S. A. Bhave, and G. D. Fuchs, Coherent control of a nitrogen-vacancy center spin ensemble with a diamond mechanical resonator, *Optica* 2, 233 (2015).
- [3] E. R. MacQuarrie, T. A. Gosavi, S. A. Bhave, and G. D. Fuchs, Continuous dynamical decoupling of a single diamond nitrogen-vacancy center spin with a mechanical resonator, *Phys. Rev. B* 92, 224419 (2015).

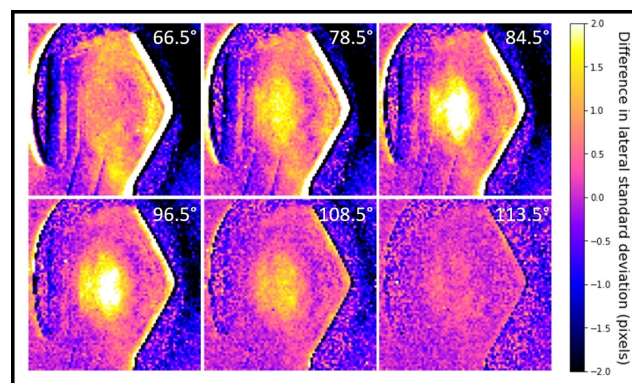


Figure 4: X-ray diffraction imaging of the FBAR. At each pixel of these two-dimensional images, there is a detector image. The standard deviation of the data in the lateral dimension is calculated. Each of the images are taken at various phases of the driving voltage to the transducer. The images are subtracted from a reference image at another phase value at 125.5°. These difference images show the mode confinement in the center of the FBAR region that appears as we introduce strain through the bulk of the diamond.

Electrochemical Thin Film Actuator Enabled Microrobots and Micromachines for Fluid Manipulation, Shape Morphing and Neural Probing

CNF Project Number: 2416-16

Principal Investigator(s): Itai Cohen, Paul L. McEuen

User(s): Qingkun Liu, Wei Wang, Jacob T. Pelster

Affiliation(s): Kavli Institute at Cornell for Nanoscale Science, Applied and Engineering Physics, Laboratory of Atomic and Solid-State Physics, Department of Physics; Cornell University

Primary Source(s) of Research Funding: National Science Foundation, Contract DMR-1719875; EFMA-1935252, Army Research Office, Contract W911NF-18-1-0032; National Institutes of Health, Grant 1R21EY033080-01

Contact: itai.cohen@cornell.edu, plm23@cornell.edu, ql59@cornell.edu, ww459@cornell.edu, jtp246@cornell.edu

Primary CNF Tools Used: Oxford ALD FlexAL, Arradance ALD Gemstar-6, Oxford 81/100 Etchers, ABM Contact Aligner, SC 4500 Odd-Hour, AJA Sputter Deposition, AJA Ion Mill, Oxford Cobra ICP Etcher, Heidelberg DWL2000, Oxford Endeavor, Oxford PECVD

Abstract:

The ability to efficiently actuate structures at the micro- and nanoscale is an essential technology for the development of microrobots and micromachines. Our team is developing a class of electrochemically driven thin film bending actuators with low voltage input and high energy density. These actuators are compatible with complementary metal-oxide-semiconductor (CMOS) technologies, which we use to interface with controlling integrated circuits. We use these actuators for three novel devices: artificial cilia that can manipulate microscale fluid fields, metamaterial robots with the ability to change shape and locomote, and a novel minimally invasive neural probe.

Summary of Research:

We developed bilayered thin film actuators that can bend in response to an electrical voltage signal [1,2]. These thin film actuators are composed of a passive layer, and an active layer, which generates strain in response to certain electrochemical reactions. Upon the application of a voltage to the active layer, the resulting strain in the active layer generates differential stresses between the two layers, triggering the actuation of bending. These actuators work in an aqueous environment and are programmable with low-voltage signals. Here we demonstrate three different applications of the actuators for developing artificial cilia [3], metamaterial robots, and neural probes.

Cilia Metasurfaces for Electronically Programmable Microfluidic Manipulation. Ciliary pumping is a powerful strategy many microorganisms use to control and manipulate fluids at the microscale. However, the development of an efficient artificial ciliary platform that can functionally manipulate fluids remained elusive.

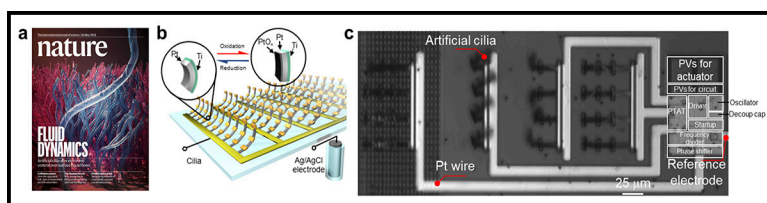


Figure 1: Current and proposed artificial cilia platforms. a) Electronically actuated artificial cilia featured in the May 26th issue of Nature. b) Electrochemical mechanism of cilia. c) Phase delayed actuation of CMOS circuit integrated cilia arrays.

Utilizing the thin film electrochemical actuators, we have developed a new class of electrically controlled artificial cilia that can programmably control micro- and nanoscale flow fields (Figure 1a). These cilia are comprised of nm thin films of Pt capped on one side by Ti. By oxidizing and reducing the platinum thin film, the induced expansion and contraction with respect to the inactive capping layer drives ciliary beating, and generates a surface flow (Figure 1b). These cilia were used to create an active cilia metasurface that can generate

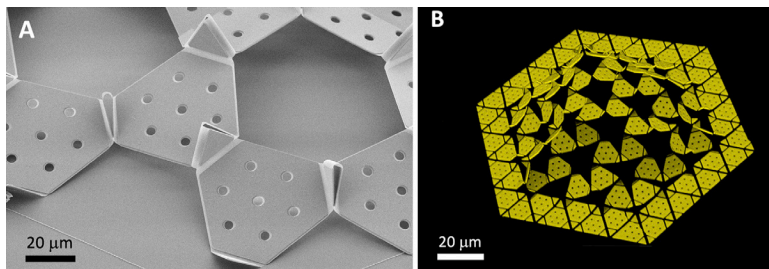


Figure 2: (a) SEM image of the active origami-inspired hinges connecting passive SiO panels. (b) Confocal image of a metarobot that transform into dome shape.

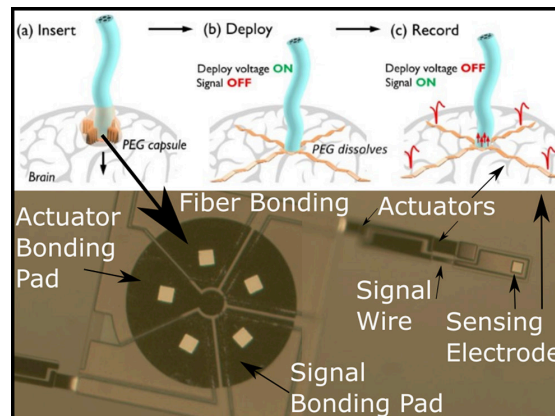


Figure 3: (Top) Schematics of the proposed probe working principle with low invasiveness. (Bottom) Structure of the prototype probe.

and switch between any desired surface flow patterns. We also integrated the cilia with a light-powered CMOS clock circuit (Figure 1c) to demonstrate wireless operation. As such, we envision numerous applications of cilia metasurfaces for fluidic manipulation with solar-powered lightweight devices in the near future.

Metamaterial-Based Microrobots. We demonstrate electrically programmable, micrometer-sized metamaterial-based robots (metarobots) that can form three-dimensional (3D) surfaces from two-dimensional patterns, cycle among different shapes, and locomote in a biocompatible solvent. These metarobots have a hierarchical structure: the repeating panels are linked by origami-based splay hinges, which are controlled by applying voltage to atomically thin surface electrochemical actuators (Figure 2A). The actuator consists of a 7 nm thick platinum layer capped on one side by a 2 nm titanium layer. Under application of potentials in the range of 1 volt, ions oxidize the platinum, create a differential in stress between the two sides, and cause the structure to bend. The splay hinge contains a single mountain and two valley folds, which convert the out-of-plane bending of the nanoactuator into in-plane rotation of the panels. When we apply a voltage, the local expansions of the unit cells alter the local Gaussian curvature of the metarobots, allowing it to reconfigure into a 3D surface. We used confocal optical microscopy to image the 3D structures of the metarobots (Figure 2B). The Gaussian and mean curvatures are then calculated from the experimental 3D images. We show that the metarobots can transform into a rich class of 3D shapes by locally actuating different subsets of the splay hinges. As a demonstration, if the inner region of the sheet is activated, the metarobot morphs into a dome shape, whereas if the outer region is activated, it transforms into a saddle shape. Furthermore, by applying a phase delay between the actuation signals of different parts of the metarobot, we break both the spatial and temporal symmetry, and drive the metarobots to locomote in a biocompatible solution.

Extendable Neural Probes. Neural probes have cemented themselves in the minds of researchers and medical practitioners as a valuable instrument with multiple applications ranging from early detection of chronic disease, to brain stimulation and prosthetic interfaces. However, conventional probes are fabricated as thin, long structures inserted perpendicular to the surface of the brain. If transverse measurement is desired, multiple probes must be inserted as an array, requiring the removal of the skull over the entire recording area. One approach to minimizing the area of skull removed is to develop a deployable probe, which actuates after insertion to increase the area of transverse measurement. Such an approach requires the use of actuators that can generate enough force to achieve transverse motion through biological tissues. We developed such an actuator based on a bilayer structure of palladium and titanium, which can now be combined with a series of 120 μm wide fiber probes, signal wires, and rigid panels to create a deployable probe. Our vision is that the entire device will be released from the substrate, and inserted into the brain in one hole only slightly larger than the (contracted, 150 μm) probe. The device will then expand transversely into the brain, allowing a much larger measurement area than the invasive area (Figure 3 top).

References:

- [1] Miskin, M. Z.; Cortese, A. J.; Dorsey, K.; Esposito, E. P.; Reynolds, M. F.; Liu, Q.; Cao, M.; Muller, D. A.; McEuen, P. L.; Cohen, I., Electronically integrated, mass-manufactured, microscopic robots. *Nature* 2020, 584 (7822), 557-561.
- [2] Liu, Q.; Wang, W.; Reynolds, M. F.; Cao, M. C.; Miskin, M. Z.; Arias, T. A.; Muller, D. A.; McEuen, P. L.; Cohen, I., Micrometer-sized electrically programmable shape-memory actuators for low-power microrobotics. *Science Robotics* 2021, 6 (52), eabe6663.
- [3] Wang, W.; Liu, Q.; Tanasijevic, I.; Reynolds, M. F.; Cortese, A. J.; Miskin, M. Z.; Cao, M. C.; Muller, D. A.; Molnar, A. C.; Lauga, E., Cilia metasurfaces for electronically programmable microfluidic manipulation. *Nature* 2022, 605 (7911), 681-686.

Synchronization and Bistability in Coupled Opto-Thermal MEMS Limit Cycle Oscillators

CNF Project Number: 2732-18

Principal Investigator(s): Prof. Alan T. Zehnder

User(s): Aditya Bhaskar

Affiliation(s): Sibley School of Mechanical and Aerospace Engineering, Cornell University
Primary Source(s) of Research Funding: NSF United States, grant number CMMI-1634664
Contact: atz2@cornell.edu, ab2823@cornell.edu
Primary CNF Tools Used: Heidelberg Mask Writer - DWL2000, Hamatech Hot Piranha, DISCO Dicing Saw, GCA 6300 DSW 5X g-line Wafer Stepper, Unaxis 770 Deep Si Etcher, Anatech Plasma Asher, Leica CPD300 Critical Point Dryer, Zygo Optical Profilometer, Zeiss Supra SEM

Abstract:

In this work, we study the nonlinear dynamics of pairs of mechanically coupled, opto-thermally driven, MEMS limit cycle oscillators. We vary three key parameters in the system — frequency detuning, coupling strength, and laser power, to map the device response. The coupled oscillators exhibit states such as the self-synchronized state, quasi-periodic state, drift state, and bistability. Specifically, we show that the laser power can be used to change the effective frequency detuning between the oscillators and at high laser powers the system shows irregular oscillations due to the existence of bistable states and sensitive dependence on system parameters.

Summary of Research:

Coupled oscillators at the microscale exhibit strong nonlinearities owing to the large deformations relative to the device dimensions [1]. This makes them suitable as experimental testbeds to study nonlinear dynamics. We study clamped-clamped beams that are nominally $40\ \mu\text{m}$ long, $3\ \mu\text{m}$ wide and $205\ \text{nm}$ thick. Frequency detuning is introduced in the system by varying the lengths of adjacent oscillators and coupling is affected by short bridges between the devices as well as elastic

overhangs near the anchor points. The bridges are spaced apart by $3\ \mu\text{m}$ and are simultaneously excited into limit cycle oscillations using a single continuous wave laser beam at a wavelength of $633\ \text{nm}$. The resonator structure forms a Fabry-Perot interferometer where the absorbance and reflectance are modulated with the cavity gap. The interference setup allows for the driving and detection of oscillations [2]. A top-view of a sample device with the edges outlined and the laser beam aligned is shown in Figure 1.

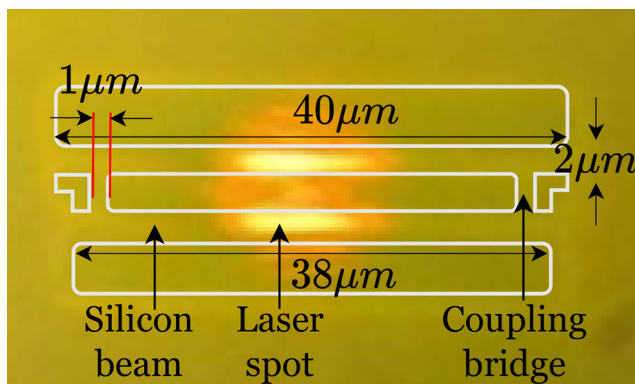


Figure 1: Optical microscope image of a sample device with the beams outlined and key dimensions labelled. The silicon device layer thickness is $205\ \text{nm}$. The laser spot aimed at the center of the device is used to drive and detect oscillations.

For plotting the synchronization region, the laser power was kept constant at approximately $1.3\ \text{mW}$ striking the devices. The spectral responses were recorded for 25 different devices. These consisted of pairs of oscillators at five different coupling and five detuning levels. In all 25 devices, the reference oscillator was of length $38\ \mu\text{m}$. The other oscillators in the pair were of length $\{42, 40, 38, 36, 34\}$ microns corresponding to a minimally coupled frequency detuning percentage of $\{-18\%, -10\%, 0\%, +10\%, +14\%\}$ respectively. A heat map of the difference in frequencies between the two oscillators for the 25 different devices is shown in the 5×5 grid in Figure 2. The plot shows a region of synchronization with boundaries marked in white. The spectra corresponding to three different dynamical states are also shown.

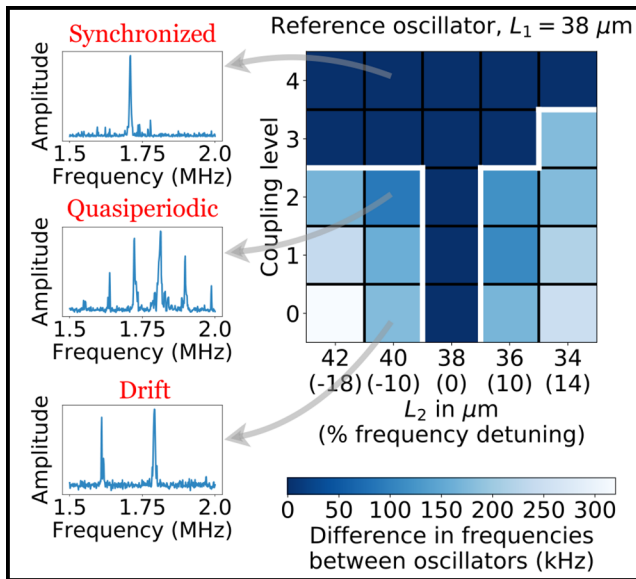


Figure 2: Experimental results showing the difference in limit cycle frequencies between pairs of oscillators in the frequency detuning vs. coupling strength space forming an Arnold tongue region of synchronization. The spectra of the system show drift, quasi-periodic, and synchronization states.

At low coupling, the oscillators are drifting with two prominent peaks in the spectrum. At moderate coupling strengths, the system shows quasi-periodic behavior with multiple sidebands in the spectrum in addition to two prominent peaks. This is the result of amplitude modulation of the oscillators due to the coupling.

At higher coupling strengths, inside the Arnold tongue region, the oscillators synchronize and the spectra collapses to a single prominent peak corresponding to the frequency of locking.

We also studied the device response at a fixed frequency detuning of -10% and by varying the coupling strength and laser power [3]. The resulting map is shown in Figure 3.

At minimal coupling, the devices exhibit a drift response for all laser powers. We note that the limit cycle frequencies decrease with an increase in laser power due

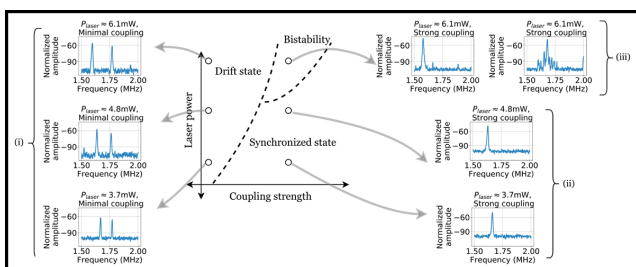


Figure 3: A map of the experimentally recorded dynamics of a pair of coupled MEMS oscillators (i) drift state at minimal coupling strengths, (ii) synchronized state in the presence of strong coupling at low laser powers, and (iii) co-existence of two stable states, i.e. synchronized oscillations and quasi-periodic oscillations in the presence of strong coupling at high laser powers.

to the strong amplitude softening behavior of the post-buckled beams, but the frequency detuning between the oscillators increases with an increase in laser power. This implies that the frequency detuning between the oscillators can be varied using the continuously varying laser power parameter.

At strong coupling, the oscillators show synchronized oscillations at low and moderate laser powers. At high laser powers, the system shows irregular oscillations with the system switching between two stable states: the synchronized state and the quasiperiodic state rapidly, due to the presence of noise in the system such as an unstable laser source. The system switching between the two states and exhibiting a broadband spectrum in the intermediate time is shown in Figure 4.

Conclusions and Future Steps:

In this work, we charted the behavior of pairs of coupled opto-thermally driven oscillators in the coupling, detuning, and laser power parameter space. The rich dynamics exhibited by such devices furthers our understanding of nonlinear oscillations and may have utility in devices such as sensors, filters, oscillator-based computers, and time-keeping devices.

References:

- [1] S. Tiwari and R. N. Candler, "Using flexural MEMS to study and exploit nonlinearities: A review," Journal of Micromechanics and Microengineering, vol. 29, no. 8, Aug. 2019, Art. no. 083002.
- [2] Blocher, David. "Optically driven limit cycle oscillations in MEMS." Cornell Thesis, <https://hdl.handle.net/1813/31202> (2012).
- [3] A. Bhaskar, M. Walth, R. H. Rand, and A. T. Zehnder, "Bistability in coupled opto-thermal micro-oscillators," Journal of Microelectromechanical Systems, (to appear) 2022.

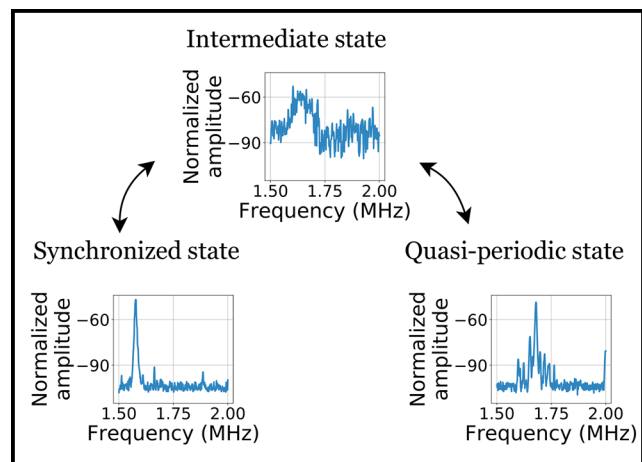


Figure 4: Bistability manifests as a broad-band spectral response in strongly coupled oscillators in the experiments (center). The oscillators rapidly switch between the synchronized state (left) with a single prominent peak in the spectrum, and the quasi-periodic state (right) with multiple satellite peaks, due to sensitive dependence of the system on the dynamical variables.

Reconfigurable Waterbomb Antenna

CNF Project Number: 2851-19

Principal Investigator(s): Robert Shepherd

User(s): Hyeon Seok An

Affiliation(s): Mechanical and Aerospace Engineering, Cornell University

Primary Source(s) of Research Funding:

Contact: rfpshepherd@gmail.com, ha259@cornell.edu

Primary CNF Tools Used: AJA Sputter Deposition

Abstract:

Up to this point, our research has focused on the materials and mechanisms for dynamic actuation of waterbomb antenna structures. Specifically, we focused on the selection of materials for foldable liquid metal (LM) joints to maintain conductivity between faces. Due to the demand for integrating multiple wireless standards into a single wireless platform, a reconfigurable antenna, also known as a tunable antenna, is attracting much attention. In mechanically reconfigurable antennas, the antenna structures consist of movable parts. In order to enable the electrical operation and mechanical reconfiguration, the antenna pieces are connected by foldable joints. In this project, an elastomer joint filled with LM was used to connect the waterbomb antenna pieces (see Figure 1a and 1b).

Summary of Research:

LMs such as gallium (Ga), eutectic gallium-indium alloy (EGaIn), or gallium-indium-tin alloy (Galinstan) are intrinsically stretchable (Dickey et al., 2008). However, Ga atoms from EGaIn spontaneously penetrate from the EGaIn to the region of the metal pad of the antenna. Moreover, it decreases the conductivity of the metal. It is possible to prevent penetration by using a thin metal layer that serves as a sacrificial layer.

The sacrificial layer absorbs the Ga atoms from EGaIn and traps them within. Ga atoms cannot transfer to the next metal layer (the thick copper layer of the antenna), preventing it from being damaged.

We used a sputtered 100 nm Au layer (sacrificial layer) above a 20 nm Cr layer (adhesion layer) to provide penetration protection. To investigate the durability against repetitive folding and releasing, the resistance of the joint was measured during cyclic bending (1,000 cycles of 45° bending angle) (see Figure 1c). The resistance remains almost constant throughout this test.

Mechanically reconfigurable waterbomb antennas were demonstrated by connecting eight waterbomb antenna pieces using eight foldable joints. An external force can control the folding angle of the waterbomb antenna, and the structure is tunable (see Figure 1d).

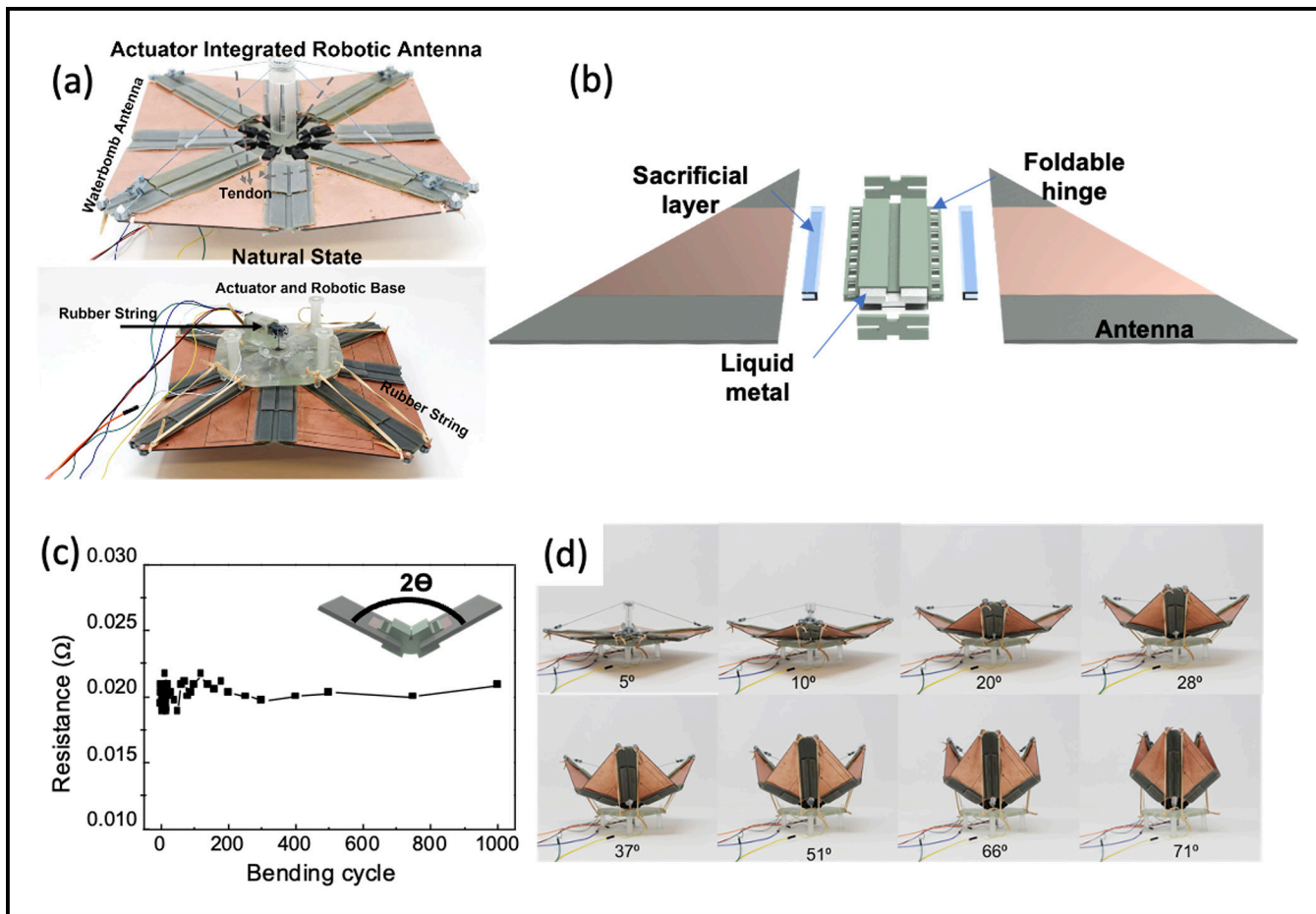


Figure 1: (a) Photograph of the waterbomb antenna. (b) Schematic image of two waterbomb pieces and a foldable joint. (c) Bending cyclic test (bending angle: 45°). (d) Photographs of the waterbomb antenna with the different folded states.

Fabrication of Micro Scale Triboelectric Generator

CNF Project Number: 2929-21

Principal Investigator(s): Shahrzad Towfighian

User(s): Mohammad Alzgool

Affiliation(s): Mechanical Engineering, Binghamton University

Primary Source(s) of Research Funding: National Science Foundation Grant #1919608

Contact: stowfigh@binghamton.edu, malzgoo1@binghamton.edu, mmalzgooll4@gmail.com

Primary CNF Tools Used: YES Asher, AJA Sputter Deposition, Heidelberg DWL-2000 Mask Writer, Oxford PECVD, Oxford 81 Etcher, PT770 Etcher, DISCO Dicing Saw, SÜSS MA6-BA6 Contact Aligner, YES Polyimide Curing Oven, Primaxx Vapor Etcher

Abstract:

Energy harvesting became of extreme importance as advances on internet of things are made. Although triboelectric generators (TEGs) are extensively researched in meso-scale as devices to harvest mechanical energy, research on downsizing TEGs to micro-scale is scarce [1]. In this project, we created and investigated the performance of a micro-scale TEG operating in contact-separation mode. The fabricated device was used as an accelerometer for accelerations in the range of 1-3 g.

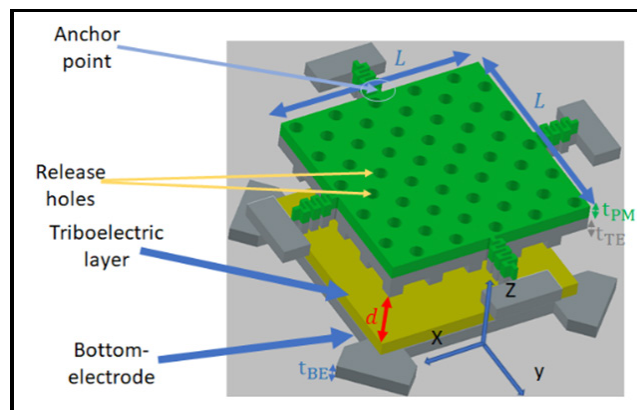


Figure 1: Micro triboelectric generator schematic.

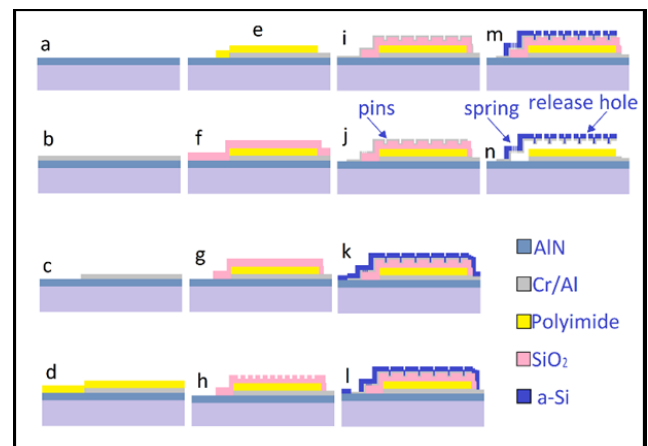


Figure 2: Micro triboelectric generator fabrication process flowchart.

Research Summary:

Triboelectric generators (TEGs) are researched nowadays because of their advantages over piezoelectric generators such as low cost, flexibility, and their high output. The triboelectric generator operating in contact-separation mode typically has three layers, two layers of which forms a triboelectric pair, and the third layer is a conductive layer that hits the substrate as shock is applied (Figure 1). Once the conductive electrode contacts the dielectric material, both layers in contact will gain/lose electrons which creates potential difference when these layers are separated. In our work, the triboelectric pair is made of polyimide (using HD microsystems PI2574 precursor) and aluminum, and the top electrode is made of aluminum too [2].

Fabrication:

The fabrication process started with sputtering 200 nm chrome/ aluminum on 1.5 μm aluminum nitride insulating layer (Figure 2 a, b). Then the chrome/ aluminum layer is patterned using PT770 etcher (Figure 2 c). Then polyimide layer was formed by spin-coating the precursor and baking it on a hot plate for 1 min followed by oven curing in the YES polyimide oven for 1.5 hours (Figure 2d). Then the polyimide was patterned using Oxford 81 etcher with CF_4/O_2 recipe (Figure 2e) [3]. This process was followed by PECVD film of SiO_2 deposited to create a gap (Figure 2f). This film was etched twice using Oxford 81 with different masks to create ditches on the top (Figure 2g,h). Then, another sputtered chrome/ aluminum film of 120 nm

was deposited on top of the oxide layer (Figure 2i), this film will have pins when it fills the ditches created on the oxide layer. This layer was etched to form top layer and springs (Figure 2j). Then, a-Si layer is deposited on top to create a proof-mass and a structural layer on top of the chrome/ aluminum (Figure 2k).

Parameters for a-Si deposition were chosen such that the resulted film stress of a-Si and chrome/ aluminum is tensile and less than 180 MPa to avoid breakage in the serpentine springs. Then, a-Si on contact pads is etched using Oxford 81 (Figure 2l), and both a-Si and chrome/ aluminum are etched to form release holes for vapor hydrofluoric acid etching (Figure 2m). Finally, dicing and releasing of the chips with vapor HF etching to remove the oxide layer was done to create micro-scale triboelectric generator (Figure 2n).

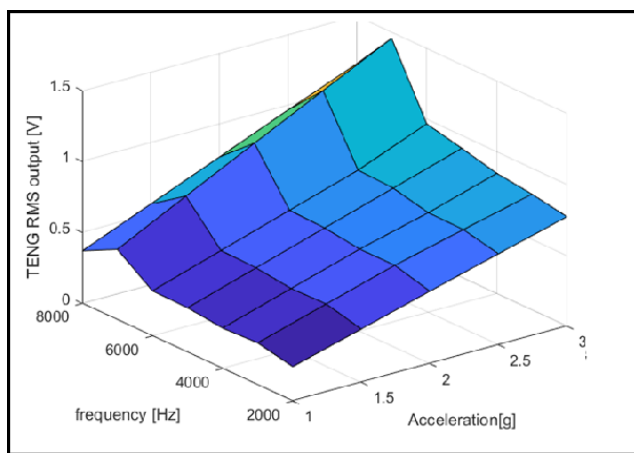


Figure 3: The relation between frequency, acceleration, and generated voltage.

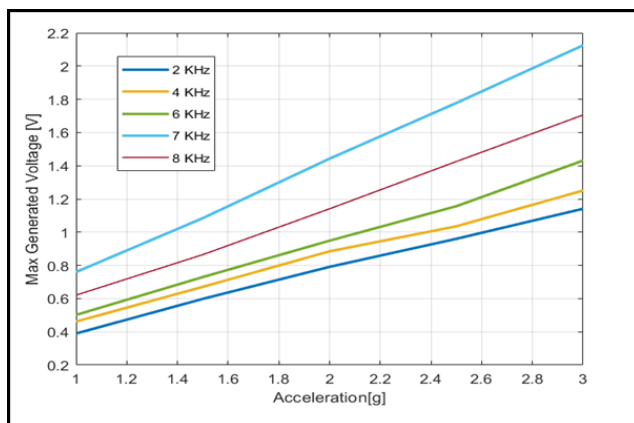


Figure 4: Generated output against acceleration with different input frequencies.

Results:

The fabricated device was mounted on a mini-shaker (B&K 4810) and an accelerometer was attached to the stage to measure the acceleration. Then the shaker was excited sinusoidally with acceleration in the range of 1-3 g. The output of the micro triboelectric generator as a function of acceleration and input frequency is shown in Figure 3. The generated voltage is noticed to be linear against acceleration at any given frequency as show in Figure 4. The sensitivity of the fabricated TENG varies as frequency is changed from ~ 0.4 V/g to ~ 0.65 V/g, which is higher than the sensitivity of the commercial accelerometer used. The highest sensitivity value is seen at the frequency of 7 KHz.

Conclusions and Future Steps:

There are plenty of parameters that could be optimized in this work. For instance, the polyimide was used here because it can withstand the 300-400°C temperature of the PECVD process while other materials like PDMS would evaporate, the output voltage might improve if we found a way to use PDMS instead of polyimide. Also, the amorphous silicon film was used here because the stress can be tuned to overcome the compressive stress of the chrome/ aluminum sputtered film. If we could swap the a-Si with a thicker conductive material and get neutralized film stress, it is possible to get higher voltage output from the reported device.

References:

- [1] H. A. Hamid, Z. Celik-Butler, Design and optimization of a mems triboelectric energy harvester for nano-sensor applications, in: 2019 IEEE Sensors Applications Symposium (SAS), IEEE, 2019, pp. 1-6.
- [2] H. Zhang, L. Quan, J. Chen, C. Xu, C. Zhang, S. Dong, C. Lu, and J. Luo, A general optimization approach for contact-separation triboelectric nanogenerator, Nano energy, vol. 56, pp. 700-707, 2019.
- [3] G. Turban, M. Rapeaux, Dry etching of polyimide in o 2-cf 4 and o 2-sf 6 plasmas, Journal of the Electrochemical Society 130 (11) (1983) 2231.

Programmable Microscopic Magnetic Self-Assembly

CNF Project Number: 2964-21

Principal Investigator(s): Itai Cohen, Paul L. McEuen

User(s): Zexi Liang, Melody Xuan Lim, Tanner Pearson, Conrad Smart

Affiliation(s): Kavli Institute at Cornell for Nanoscale Science, School of Applied and Engineering Physics, Laboratory of Atomic and Solid-State Physics, Department of Physics, Cornell University; School of Engineering and Applied Sciences, Harvard University.

Primary Source(s) of Research Funding: This work was supported by NSF grant DMR-1921567, Sloan Foundation-Contract G-2021-14198

Contact: itai.cohen@cornell.edu, plm23@cornell.edu, brenner@seas.harvard.edu, zl467@cornell.edu, mxl3@cornell.edu, tgp34@cornell.edu, cs2239@cornell.edu

Primary CNF Tools Used: Oxford 81/82 Etcher, Oxford 100 Etcher, ASML DUV Stepper, JEOL 6300 EBL, SC 4500 Odd-Hour Evaporator, AJA Sputter, Oxford PECVD, Heidelberg Mask Writer - DWL2000, PT770 Etcher, Unaxis DRIE, Plasma-Therm DRIE, Zeiss SEM, Veeco AFM

Abstract:

We are developing a microscopic self-assembly system with programmable magnetic interactions. In order to encode specific magnetic lock-and-key interactions between pairs of micron-scale particles, we embed nanoscale single-domain magnets along their perimeters, and program their magnetic configurations. When these non-equilibrium particles are magnetically and hydrodynamically driven to explore their configuration space, they self-assemble into complex structures, as encoded by the embedded magnetic information.

Summary of Research:

Self-assembly refers to a group of ubiquitous processes that turns a disordered system of dispersed building blocks into organized structures or patterns via local interactions between the building blocks with minimal external guidance. Among various kinds of local interactions that can lead to self-assembly, the magnetic interaction is unique for its scalability across multiple scales from sub-micrometer to macroscopic. Previously, we have shown that macroscopic polymer particles with embedded permanent magnets can self-assemble via programmable magnetic interactions into 1D polymers, 2D square lattices and even 3D cage structures [1]. Based on the scalable nature of magnetic interactions, we are now developing magnetically programmable particles with information encoded in the magnetic patterns to achieve self-assembly in a controlled manner at the microscale.

We have fabricated microscale panels with magnetic patterns embedded in silicon oxide thin films as building blocks for programmable magnetic self-assembly (Figure 1a,b). Sub micrometer single-domain nanomagnets that are pill shaped and have various aspect ratios are patterned via electron beam lithography followed by metallization of cobalt and liftoff. Since the nanomagnet coercivity is directly controlled by its aspect ratio, we

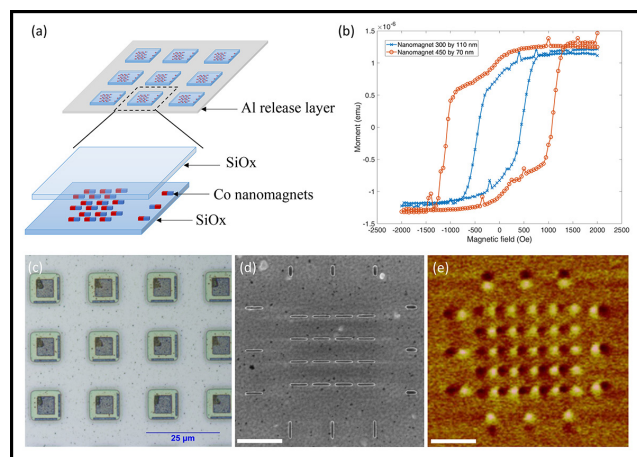


Figure 1: Magnetically programmable self-assembly at water-air interface. (a-b) schematics and optical image of the magnetic panels. (c-d) SEM and MFM images of the magnetic panels. Scale bar: 1 μ m.

can fabricate domains with small and large magnetic coercivity which allows us to control the domain magnetization through sequential application of large followed by smaller magnetic fields [2]. For instance, in order to have opposite magnetic dipoles in both x and y directions, we pattern two types of nanomagnets with different aspect ratios and coercivities.

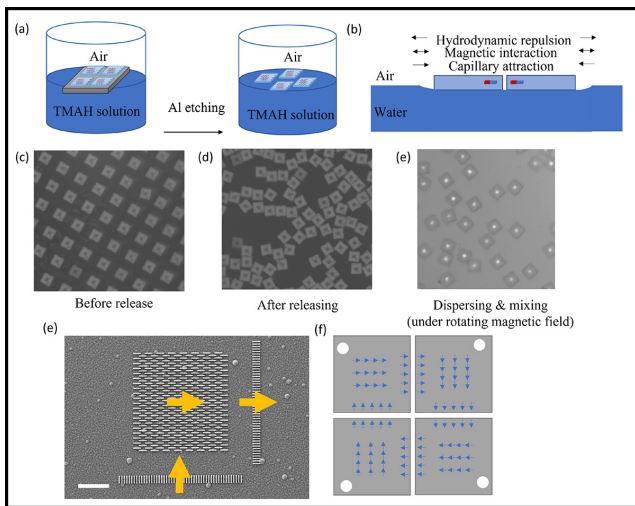


Figure 2: (a) Schematics of magnetic panels released and assembled at water-air interface. (b-e) Magnetic panels float at the water-air interface before, after releasing and mixing. (f) SEM of nanomagnets pattern for self-limiting assembly. Scale bar: 2 μm . (g) Schematic of a tetramer assembled from four identical magnetic panels.

All the magnets are first magnetized (in both x and y directions) using a magnetic field higher than the coercive fields for both domains. Subsequently, the shorter domains are magnetized in the opposite directions using a coercive field whose intensity is high enough to flip the short domains but too weak to flip the long domains. In this way, we produce near-field interactions between adjacent magnetic panels with programmable selectivity.

By introducing lock and key pairs of magnetic handshake patterns into the design of patterns, we aim to generate specificity in magnetic bindings [1,3]. Utilizing the specificity of magnetic bindings, we could further design more complex self-assembled structures such as polymers with unique properties and functionalities and even self-assembled magnetic micromachines. Finally, in addition to these near-field interactions, we control the panel far-field interactions by patterning a large central array of magnets (see Figure 1a). This central array of magnets also provides a means to actuate the magnetic panels with an external magnetic field.

The panels are fabricated on a suspended thin sacrificial layer made of aluminum. We release the panels for self-assembly by floating the panels and sacrificial layer on top of a tetramethylammonium hydroxide (TMAH) solution. The TMAH etches the aluminium layer, leaving the magnetic panels free-floating in a single layer, on an effectively frictionless two-dimensional surface (Figure 2a). We design the shape and size of the magnetic panels so as to minimize the distortion of the liquid interface caused by the panels, thus isolating the forces driving assembly to the magnetic patterns on the panel edge.

The very low friction environment of the liquid interface enables us to visualize the effect of small magnetic forces, as well as to introduce out-of-equilibrium driving.

In particular, to allow the panels to effectively explore their configuration space, we spin the panels using a rotating external magnetic field. As the particles spin, the fluid around them is also forced to flow in a vortex. As the spinning speed increases, this rotating flow leads to chaotic trajectories between individual magnetic panels, so that panels “mix” and weak structures break (Figure 2b-d). For sufficiently large rotation rates (more than 10 Hz), the magnetic panels explore their configuration space until they bind in their strongest configuration (Figure 2e).

As the first proof of concept, we demonstrate that a single type of magnetically patterned square panel self-assembles into self-limiting clusters. The magnetic patterns consist of a large central magnet array as the handle for external field manipulation and mixing, and two arrays of magnets near the two adjacent edges of the panels (Figure 2f,g). When the correct binding forms, four panels will be assembled into a tetramer, with each panel rotated 90° from the adjacent one (Figure 2g).

In addition to self-assembly at the water-air interface for 2D structures, we also developed an acoustic approach that could effectively agitate the micrometer-sized particles in 3D (Figure 3a,b). We utilize surface acoustic wave (SAW) devices to generate standing surface acoustic wave (SSAW) on a lithium niobate piezoelectric substrate and then couple the wave into the microfluidic well where the magnetic particles are released (Figure 3a). The particles are manipulated by acoustic radiation force and acoustic streaming. To effectively mix the particles, we further modulate the phase of the voltage signal applied to the interdigital transducers and randomized the distribution of the pressure nodes of the SSAW. We envision that this acoustic agitation approach could be adopted in future self-assembly experiments for programmable 3D assembly of magnetic particles.

References:

- [1] R. Niu, C. X. Du, E. Esposito, J. Ng, M. P. Brenner, P. L. McEuen, I. Cohen, Proceedings of the National Academy of Sciences 2019, 116, 24402.
- [2] J. Cui, T.-Y. Huang, Z. Luo, P. Testa, H. Gu, X.-Z. Chen, B. J. Nelson, L. J. Heyderman, Nature 2019, 575, 164.
- [3] C. X. Du, H. A. Zhang, T. Pearson, J. Ng, P. McEuen, I. Cohen, M. P. Brenner, arXiv preprint arXiv:2112.02614 2021.

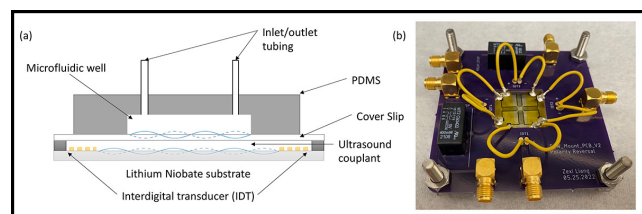


Figure 3: (a) Schematic of the surface acoustic wave setup for magnetic particle agitation in microfluidics. (b) Photo of the surface acoustic device bonded to the driving circuit board.